USING LANDMARK BASED SUSCEPTIBILITY WEIGHTED IMAGING FOR INTERVENTIONAL DEVICE LOCALIZATION IN MRI

A Thesis

by

PRANAV VAIDIK DHULIPALA

Submitted to the Office of Graduate and Professional Studies of
Texas A&M University
in partial fulfillment of the requirements for the degree of

MASTER OF SCIENCE

Chair of Committee,   Jim X. Ji
Committee Members,   Steven M. Wright
                                   Krishna R. Narayanan
                                   Jeff Huang
Head of Department,   Miroslav Begovic

August 2018

Major Subject: Electrical Engineering

ABSTRACT

MRI is a widely studied imaging modality due to its superior resolution and soft-tissue contrast. However, the application of MRI is limited in cases when metallic interventional devices are present in the target tissues. High susceptibility of metallic objects often causes artifacts in MR images, making them difficult to localize. SWI is a widely used clinical tool to enhance the image contrast in MR imaging modality. SWI uses phase information of MR images to enhance contrast in tissues with different susceptibilities. In this study, we use a novel SWI-based approach called Metal ARtifact Based Landmark Enhanced SWI (MARBLES) to create a positive contrast image (PCI) for localizing the metallic objects in the MR images. The approach was tested on four different dataset and the results were observed, discussed and compared against that of a Qualitative Susceptibility Mapping (QSM) based approach.

DEDICATION

I dedicate this work to my parents Sridhar and Satyavati, and my brother Kireeti for their constant

support and encouragement. Special thanks to my best friend Pramod for always being there for

me during my hard times.

ACKNOWLEDGMENTS

CONTRIBUTORS AND FUNDING SOURCES

Contributors

The original MRI datasets used in this research were acquired and provided by Ms. Caiyun Shi and Dr. Guoxi Xie from Shenzhen Institute of Advanced Technology (SIAT), Chinese Academy of Science. The codes for calculating the Qualitative Susceptibility Maps (QSM) were shared by Dr. Ying Dong from TAMU and Ms. Caiyun Shi. The public software from Cornel MRI Research Lab website (http://weill.cornell.edu/mri/pages/qsm.html) is also acknowledged. The time comparisons for QSM vs. MARBLES were performed with the assistance of Ms. Samira Vafay Eslahi.

All other work conducted for the thesis was completed by the student independently.

Funding Sources

NOMENCLATURE

B/CS	Bryan and College Station
CGS	Conjugate Gradient Solver
co-RASOR	center-out RAdial Sampling with Off-resonance Reception
CT	Computed Tomography
DBS	Deep Brain Stimulation
FGS	Fluorescence Guided Surgery
FOV	Field Of View
FSE	Fast Spin Echo
IRON	Inversion-Recovery with ON-resonant water suppression
LBV	Laplacian Bound Value
MARBLES	Metal ARtifact Based Landmark Enhanced Susceptibility Weighted Imaging
MAVRIC	Multiple Acquisition Variable Resonance Image Combination
MIP	Maximum Intensity Projection
MRI	Magnetic Resonance Imaging
NSF	National Science Foundation
NSFC	National Science Foundation of China
PET	Positron Emission Tomography
PCI	Positive Contrast Image
QSM	Qualitative Susceptibility Mapping
ROI	Region Of Interest
SE	Spin Echo

SEMAC	Slice Encoding for Metal Artifact Correction
SGM	Susceptibility Gradient Method
SNR	Signal to Noise Ratio
SPIO	Super Paramagnetic Iron Oxide
STFT	Short Term Fourier Transform
SUMO	SGM Using the Original resolution
SWI	Susceptibility Weighted Imaging
TAMU	Texas A&M University

TABLE OF CONTENTS

Page

LIST OF FIGURES

LIST OF TABLES

1. INTRODUCTION AND LITERATURE REVIEW

1.1 Background

Imaging often plays significant roles in surgeries involving interventional devices for various purposes such as localization of target, guidance during the surgery and post-surgery evaluation. Over the years, computed tomography (CT), positron emission tomography (PET) and ultrasound imaging have been the choice of imaging modalities for these applications due to their relatively low cost and fast acquisition.

Ultrasound imaging is one of the imaging modalities well known for its fast and inexpensive applications in imaging guided procedures. Ultrasound guided interventional procedures were used for diagnosing ailments such as liver neoplasms [1], brain tumors [2] and breast lesions [3,4]. As early as 1983, the modality was employed for guiding the brachytherapy procedure [5,6].

CT is another non-invasive modality employed for imaging guided surgeries due to its cheap cost and good image quality [7]. CT was also used to guide procedures such as biopsy [8–10], stereotactic surgeries [11], angiography [12], brachytherapy [13, 14] and deep brain stimulation [15].

PET is also an imaging modality with applications in imaging guided procedures [16]. PET was employed during the planning phase of the brachytherapy [17,18] and surgery phase of deep brain stimulation (DBS) [19]. PET and CT were also used in combination to improve interventional device localization [20].

X-ray fluoroscopy imaging is yet another modality known for its utility in image guided procedures such as gynecologic brachytherapy [21–23], cardiac catheterization [24], uteral stent exchange [25] and biopsy [26, 27]. However, the risk of radiation exposure issue due to ionizing radiation [28] and the poor tissue contrast compared to that of ultrasound imaging, CT and MRI [29] make fluoroscopy undesirable as a image guiding modality.

Imaging guided surgeries also use fluorescence imaging, popularly known as Fluorescence

1

Guided Surgery (FGS). FGS is well known for being inexpensive and also for its superior image resolution [30]. FGS was proved to be efficient for various procedures such as tumor detection [31] and cancer surgeries [32, 33]. Nevertheless, FGS often has poor penetration depth [34], as a result of using visual and near infrared (NIR) spectrum.

However, the superior soft-tissue contrast and image quality has driven scientists to explore the use of MRI in surgeries such as brachytherapy, biopsy and angioplasty. In the 1980's, MRI was explored for its application in planning phase the brachytherapy surgery [35–37]. In 2004, a detailed documented study was conducted for prostate brachytherapy surgeries with MRI being employed at every stage [38], exhibiting the feasibility of MRI as a superior guidance imaging modality. MRI was also explored for its application and safety for DBS procedures [39–41].

While the interventional devices needed to be MRI compatible for the monitoring to be feasible, most of the devices have metallic outer shells with high magnetic susceptibility. The high-susceptibility objects affect signals from the surrounding tissues by introducing fast dephasing, decreasing the signal to noise ratio (SNR), causing visible artifacts [42–44]. The affected region can be viewed as dark spots in the conventional MR images, which are often several times bigger than the objects themselves. The dark spots often make it difficult to locate the objects in the magnitude image, thus limiting its localization and assessment in MR images [38, 45]. This phenomenon also makes it difficult to differentiate the metallic objects from other dark objects in the magnitude image such as arteries, natural cavities and bones [44].

Approaches such as Slice Encoding for Metal Artifact Correction (SEMAC) [46] and Multiple Acquisition Variable Resonance Image Combination (MAVRIC) [47] were proposed to minimize the effect of the artifacts. Nevertheless, the visualization of the metallic objects themselves was not improved with these methods [48, 49].

1.2 Literature Review

Several methods were proposed to improve the metallic object visualization in MRI. The technique Inversion-Recovery with ON-resonant water suppression (IRON) [50] used a spectrally-selective on-resonant saturation pre-pulse to provide positive image contrast. A recent study intro-

2

duced a technique called center-out RAdial Sampling with Off-resonance Reception (co-RaSOR) [49] that uses off-resonance reception and shifts the signal towards the center of the object to construct a positive contrast. Further improvement was done to co-RASOR to use single acquisition and in addition to off-resonance reception [51]. However, the requirement of significant pulse sequence modification in these methods complicates their implementation using clinical MRI scanners, limiting their utility.

To address this problem, numerous post-processing methods were proposed, as they do not require pulse sequence modification. The method Susceptibility Gradient Method (SGM) [52] approached used local field map gradient to construct the positive contrast, where the gradient was calculated using Short-Term Fourier Transform (STFT) over a window. The method was later improved to replace the STFT step with a truncated filter in k-space, with the name SGM Using the Original resolution (SUMO) [53]. Nonetheless, the positive contrast regions constructed by both these approaches were much larger in area than the objects, causing potential errors in localization.

Qualitative susceptibility mapping (QSM) is another post-processing approach primarily developed and used to visualize Super Paramagnetic Iron Oxide (SPIO), iron deposition in capillaries and veins [54–56]. Despite being widely studied for visualization, a direct application of QSM methods on the MR images is limited. This is due to MRI images suffering high signal loss and rapid phase wrapping as a result of high susceptibility of metallic objects.

A novel susceptibility based positive contrast approach for visualizing brachytherapy seeds was introduced by Dong et al [57, 58], which combines both sequence developing and post-processing methods. The approach exploits the phase difference in modified spin echo (SE) sequences caused by susceptibility to compute the local field map. The susceptibility map χ is obtained from kernel deconvolution using l_1 minimization described by

$$\arg \min_{\chi, \lambda} f(\chi, \lambda) = ||W(C\chi - \Delta B)||_2^2 + \lambda ||MG\chi||_1 \qquad (1.1)$$

where C is a dipole kernel convolution operator, M and W are masking and weighing matrices respectively, ΔB is the field map and G is a first order gradient operator. An improved version

has recently been introduced to replace SE with fast spin echo (FSE) sequences, improving the acquisition speed of the MR images [59]. However kernel deconvolution and l_1 minimization usually requires high computation time.

In this study, we proposed a Susceptibility Weighted Imaging (SWI) based approach called Metal ARtifact Based Landmark Enhanced SWI (MARBLES) to construct a PCI for visualization and localization of the metallic interventional devices in MR images. SWI uses the phase information of MR images in order to enhance the contrast of the tissues with different susceptibilities. SWI recently became a very popular clinical imaging tool for visualizing and diagnosing iron deposits in brain, deoxyhemoglobin in blood, calcification etc. [60], where it uses phase information to enhance the contrast between tissues of different susceptibilities [61–63].

In our approach, we used modified SWI-based technique to highlight the metallic objects in the PCI. The technique takes into account the locations of artifacts in the local field formed due to the metallic objects and uses them to construct a region of interest (ROI) to narrow down their locations. The phase information is further used in conjunction with the ROI to construct a phase mask, followed by the construction of a PCI. The target objects can be visualized using Maximum Intensity Projection (MIP). The technique uses significantly simple mathematical approach, making it computationally faster than other approaches discussed above.

2. METHODS

2.1 Data Acquisition

Four image datasets were used for our experiments. The image acquisitions were carried out using a 3T Siemens whole-body MRI scanner with an eight-channel phased array coil. For each dataset, two datasets with and without T_{shift} were acquired using [59]. The turbo factor in the acquisitions were 7.

2.1.1 Biopsy Needle Experiment

In the first dataset, the phantom was constructed using a titanium biopsy needle inserted in a plastic container filled with distilled water. The distilled water was doped with $1.0g$ $1-1$ copper sulphate solution. The needle was $160.0mm$ long and $2.0mm$ in diameter, and was oriented parallel to the magnetic field. Scan parameters were: FOV = $80mm \times 80mm \times 80mm$, matrix size = $128 \times 128 \times 37$, TR = $2000ms$, TE = $18ms$, in-plane resolution = $0.625mm \times 0.625mm$, slice thickness = $1.5mm$, slice gap = 0.25%, bandwidth = $134Hz/Pixel$, $T_{shift} = 0.6ms$ and $0ms$. The total acquisition time was 4.0min.

2.1.2 Brachytherapy Seeds Experiment

The phantom for the second dataset was a pork tissue inserted with five dummy brachytherapy seeds at different inter-seed spacing. The dummy seeds were made of a titanium capsule which encloses a silver rod impregnated with Iodine-125. The seeds were carefully placed as perfectly oriented along the B_0 field. A cavity, a capillary and a human bone were also simulated using a plastic stick, a bamboo toothpick and a small animal bone, respectively. Acquisition of image slices was done along the coronal plane, while the seeds were oriented in the longitudinal direction. Using a modified fast-spin echo sequence, the data was acquired with the scan parameters as follows: FOV = $120mm \times 120mm \times 15mm$, matrix size = $192 \times 192 \times 10$, TR = $2000ms$, TE = $18ms$, in-plane resolution = $0.625mm \times 0.625mm$, slice thickness = $1.5mm$, slice gap = $0mm$, and bandwidth = $134Hz/Pixel$. Two datasets were obtained with echo shift of $T_{shift} = 0ms$ and

$0.6ms$.

2.1.3 Stent Experiment (Coronal)

For the third dataset, the experiments were executed on a tracheal stent, manufactured by Micro-Tech (Nanjing) Co., Ltd. The phantom is constructed by perpendicularly inserting the stent into a gelatin phantom doped with 1.0 g/L copper sulfate solution. The stent was made of Ni-Ti alloy with magnetic susceptibility $\chi_{nitinol} = 245ppm$. The dimensions of the stent were as follows: length $\times$ diameter = $60mm \times 20mm$ and wire diameter = $0.24mm$. For dataset acquisition, the axis of the stent was oriented perpendicular to the direction of the magnetic field.

Scan parameters were: FOV = $95mm \times 95mm$, voxel size = $0.3668 \times 0.3711 \times 1.5000$, matrix size = $259 \times 256 \times 17$, TR = $2000ms$, TE = $18ms$, in-plane resolution = $0.37mm \times 0.37mm$, slice thickness = $1.5mm$, slice gap = $0mm$, bandwidth = $134Hz/Pixel$, $T_{shift} = 0.6ms$.

2.1.4 Stent Experiment (Traverse)

The fourth dataset uses the same phantom from the third dataset (see section 2.1.3), where the stent in the phantom is oriented parallel to the direction of magnetic field for the dataset acquisition. Scan parameters for the acquisition were: FOV = $95mm \times 95mm$, voxel size = $0.3668 \times 0.3711 \times 1.5000$, matrix size = $259 \times 256 \times 25$, TR = $2000ms$, TE = $18ms$, in-plane resolution = $0.37mm \times 0.37mm$, slice thickness = $1.5mm$, slice gap = $0mm$, bandwidth = $134Hz/Pixel$, $T_{shift} = 0.6ms$.

2.2 Positive Contrast Image Reconstruction

The applications of susceptibility weighted imaging for MR imaging was extensively studied for several years. Haacke et al. [62] explained that the phase at the locations with metallic content such as veins, arteries and metallic interventional objects was negative, and discussed various approaches to combine magnitude and phase images for SWI.

2.2.1 Constructing Magnitude Mask

In our approach, we first obtain a magnitude mask by thresholding the magnitude image to provide us with information on the metal object locations and other conflicting objects. Since
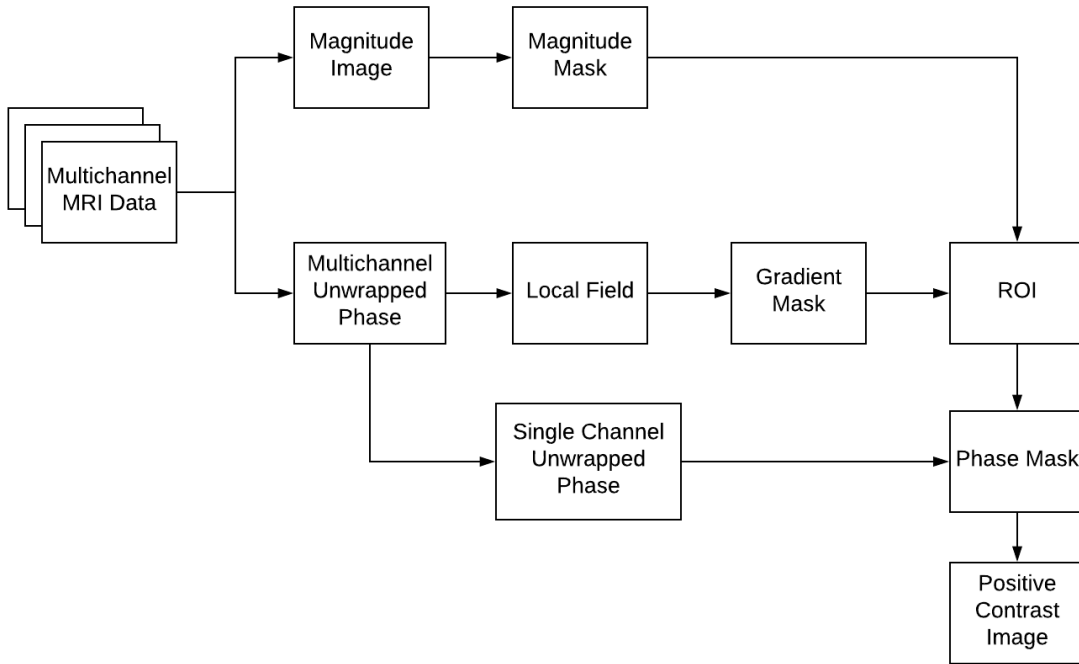
Figure 2.1: Flowchart Describing the process to create Positive Contrast Image from MR Image Data

magnitude images often have metallic objects, simulated blood vessels, cavities and bones appear as black regions [38, 64–68], the magnitude mask provides primary information on the metal target locations. Since the datasets we have are multichannel, the channels are first combined by calculating the sum of squares of the magnitude image across all the channels. This is followed by thresholding the resultant combined magnitude image. The threshold for magnitude mask was experimentally set to 20% of the maximum voxel magnitude.

2.2.2 Constructing Local Field Mask

Local field map is subsequently constructed from the phase maps according to the process described by Dong et. al [57]. The local field is calculated by removing the background noise from the field map ΔB, which is calculated according to the equation

$$\Delta B = \frac{\Delta \phi}{2 \gamma B_0 \Delta T_{shift}} \qquad (2.1)$$

where ϕ is the unwrapped phase of the image at each voxel, $\Delta \phi$ is the corresponding unwrapped phase difference of the two spin-echo sequences, ΔT_{shift} is the difference in echo shifts of the two images, γ is the gyromagnetic constant, and B_0 is the magnetic field strength using which the images were acquired. The background field is removed from the field map using Laplacian Bound Value (LBV) [57, 69] to obtain the local field.

Since artifacts due to metallic objects are also formed in phase images, they are often present in the calculated local field as well. Since these are not formed around the other conflicting objects, the artifacts can be used as landmarks for estimating the neighborhood locations of the metallic objects. A reliable method for obtaining the neighborhood is to threshold the gradient of the local field, followed by morphological dilation. In our experiments, we have used 3×3 Laplace filter to calculate the local field gradient. The threshold for local field mask was set to 40% of the maximum magnitude of local field gradient. The morphological dilation was performed using a strel kernel with diameter of 3 pixels.

2.2.3 Construction of ROI

From both the magnitude and local field masks, a common region indicating the locations of the metallic objects is obtained. Hence a Region of Interest (ROI) is constructed by performing the logical AND of magnitude and field map masks. The ROI excludes the dark spot locations formed due to conflicting objects, as these objects do not induce artifacts. Thus, ROI indicates regions that are in the vicinity of the artifact regions and also appear dark in the magnitude image, providing us with the neighborhood of only metallic objects, while excluding the conflicting objects.

2.2.4 Phase Mask Construction

Before constructing the phase mask, we combine all the channels in the MR image to obtain the combined phase $\Theta(x)$. Due to rapid phase wrapping and low magnitude, the phase information in the vicinity of the seeds are unreliable. The assumption is based on the fact that low SNR is

yielded by a low magnitude signal, thus making it more unreliable. Thus, to lower the weight on unreliable information around the seeds, we use magnitude image as weights for combining the phase, according to

$$\Theta(x) = \angle(\frac{1}{C}\sum_{c=1}^{C} e^{j\theta_c(x)} M_c(x)) \tag{2.2}$$

where C is the number of channels, $\theta_c(x)$ and $M_c(x)$ are the phase and magnitude images for channel c. This is followed by unwrapping the combined phase using LBV.

Finally, a phase mask is constructed in a manner similar to Haacke et al. [61, 62]. The use of High Pass (HP) filtering step as mentioned in [62, 63, 70] was found to result in loss of important phase information by removing the metal object artifacts. We hence use the information obtained from the ROI and the phase image obtained from equation(2.2) to construct a phase mask defined in equation (2.3). The phase mask function $g(x)$ is defined to enhance the metal object locations while suppressing all other locations as follows:

$$g(x) = \begin{cases} \frac{-1.5\pi+\phi(x)}{\pi}, & \text{for } -\pi < \phi(x) < 0 \text{ and } x \in ROI \\ 0.5, & \text{otherwise} \end{cases} \tag{2.3}$$

where $\phi(x)$ is the unwrapped phase image at x. The function $g(x)$ enhances the voxels with negative phase in the ROI and suppresses the rest of the voxels.

2.2.5 PCI Reconstruction

The contrast in the phase mask can be enhanced by multiplying the phase mask with itself as many times (integer m) as required to construct a positive contrast image $I(x)$, according to

$$I(x) = g^m(x) \tag{2.4}$$

where $I(x)$ is the PCI constructed from the phase mask, m is the tuning parameter for adjusting the contrast as required in the PCI. In our experiments, we have set the value of m to 8.

9

2.2.6 Computational Complexity

Computational complexity calculations for QSM and MARBLES were estimated assuming the input to be the local field map and output as PCI for both approaches.

The computational complexity of QSM approach mentioned in [57] was estimated to be of the order $O(pN \log N)$, described in appendix A, where N is the MR image size and p is the number of operator calls made to calculate terms in equation (A.2).

For MARBLES, we first estimate the complexity of the magnitude mask construction. The construction of magnitude mask involves simple thresholding, making it an operation with complexity order of $O(1)$.

For Local Field Mask construction, the Laplace filter, thresholding and morphological dilation operations are taken into account for computational complexity calculations. Since Laplace filter operation is a two-dimensional convolution operation, the complexity of its operation is $O(qN)$, where q is the size of the Laplace filer. Thresholding and dilation operations are $O(1)$ and $O(N)$ operations respectively. Thus, the complexity of constructing the local field map is $O(qN) + O(1) + O(N) = O(qN)$.

Hence, on comparing the respective complexities for both approaches, we see that MARBLES has theoretically lower computational complexity for PCI construction.

3. RESULTS AND DISCUSSION

The experiments were performed on 4 datasets to compare the performance of QSM vs. MARBLES. All the QSM calculations were performed using the methods described in Shi et al. [59] Qualitative Susceptibility Maps (QSM) for the datasets were computed and compared against our results. Figures 3.1, 3.2, 3.3 and 3.4 demonstrate the experimental results with puncture, seeds and both stent (coronal and traverse) datasets respectively.

Simulations and computation time comparisons were implemented using a computer in MATLAB version R2017b environment running in 64-bit Windows 10 operating system. The computer was equipped with 16 GB of RAM and Intel Core i7-7500U processor.

3.1 Experiments with Biopsy Needle

Figure 3.1 shows the comparison of results of MARBLES vs. QSM for puncture data. The center (20th) slice of the dataset was used for slice comparisons and the MIP was used to compare the shape retention of the biopsy needle. Figure 3.1d shows the local field mask generated by thresholding the gradient of local field map, followed by morphological dilation. Figure 3.1e shows the ROI constructed from the local field mask and the magnitude mask. It can be observed that the ROI construction significantly narrows down the search for the target region, as the target objects are often in the neighborhood of the artifact locations. Figure 3.1h demonstrates the localization of the biopsy needle using MARBLES marked in green on the magnitude image slice. MIP comparison for both MARBLES (Figure 3.1j) and QSM (Figure 3.1i) shows that the shape of the needle is preserved with MARBLES approach.

3.2 Experiments with Brachytherapy Seeds

Figure 3.2 shows the comparison of results of MARBLES vs. QSM for the Seeds dataset. For slice comparisons, the 4th slice of the dataset where the seeds are found was used. The Seeds dataset is a more interesting dataset for the experiment, as it contains multiple target objects and conflicting objects that can cause dark regions in the magnitude image. Figure 3.2a shows a picture

11

(a)　　　　(b)　　　　(c)　　　　(d)

(e)　　　　(f)　　　　(g)　　　　(h)

(i)　　　　　　　　　　　　(j)
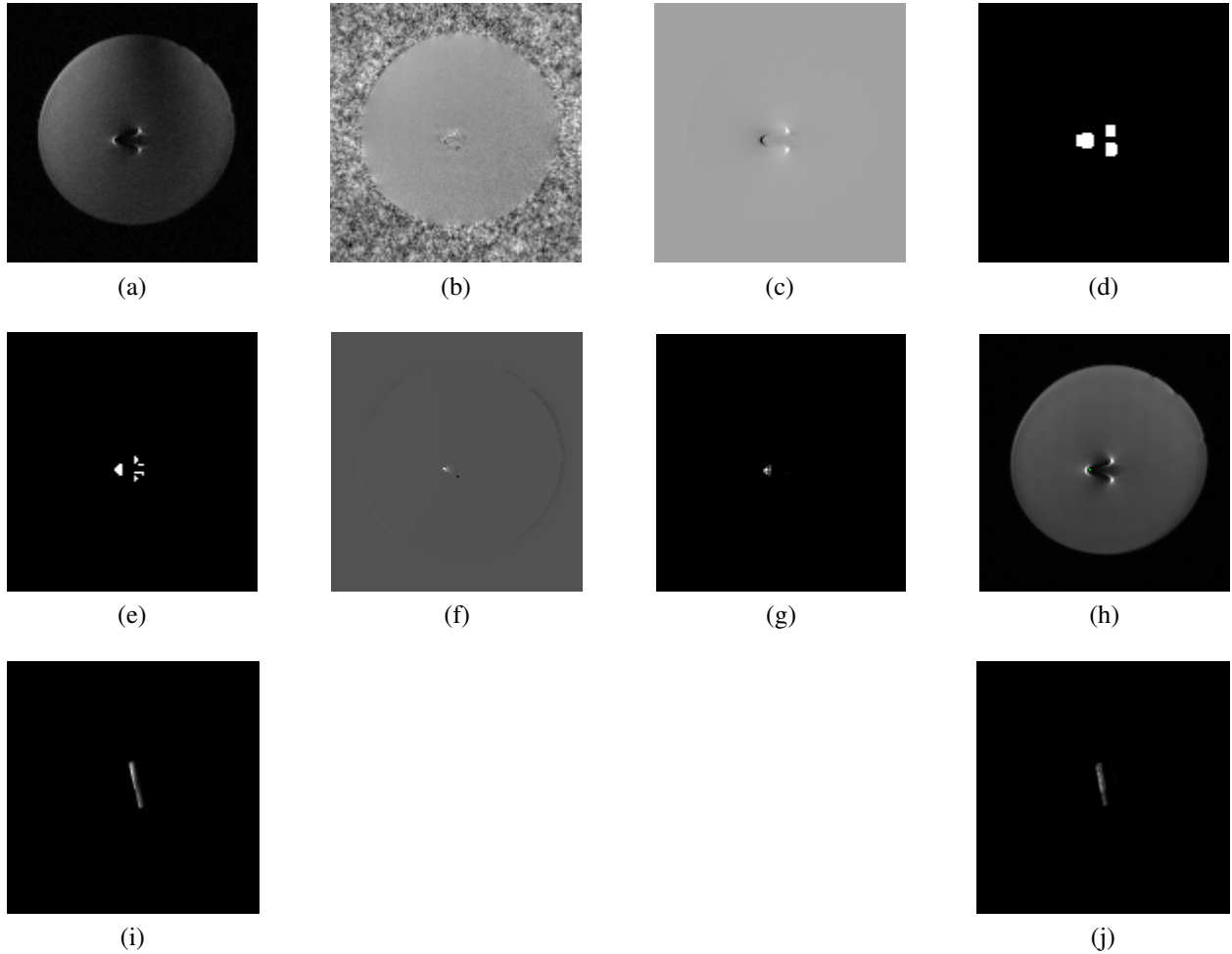
Figure 3.1: Representative reconstructions from data acquired using the phantom with a biopsy needle. (a) Magnitude image (slice 20); (b) Unwrapped Phase Image (slice 20); (c) Local Field Map (slice 20); (d) Local Field Mask (slice 20); (e) ROI (slice 20); (f) PCI generated using QSM (slice 20); (g) PCI generated using MARBLES (slice 20); (h) Needle location marked in Magnitude Image (slice 20); (i) MIP for QSM (j) MIP for MARBLES

of the tissue phantom with positions of all the seeds and conflicting objects such as the plastic stick, bamboo stick and animal bone marked and labeled. The seeds in the phantom are placed with the spacing between them marked in figure 3.2a as $L_1 = 5mm$, $L_2 = 15mm$ and $L_3 = 10mm$ respectively. Magnitude image, as shown in figure 3.2b shows dark areas that are not caused by the metallic seeds such as a plastic stick, bamboo toothpick and a small animal bone simulating the presence of a cavity, capillary and a bone in the tissue, respectively.
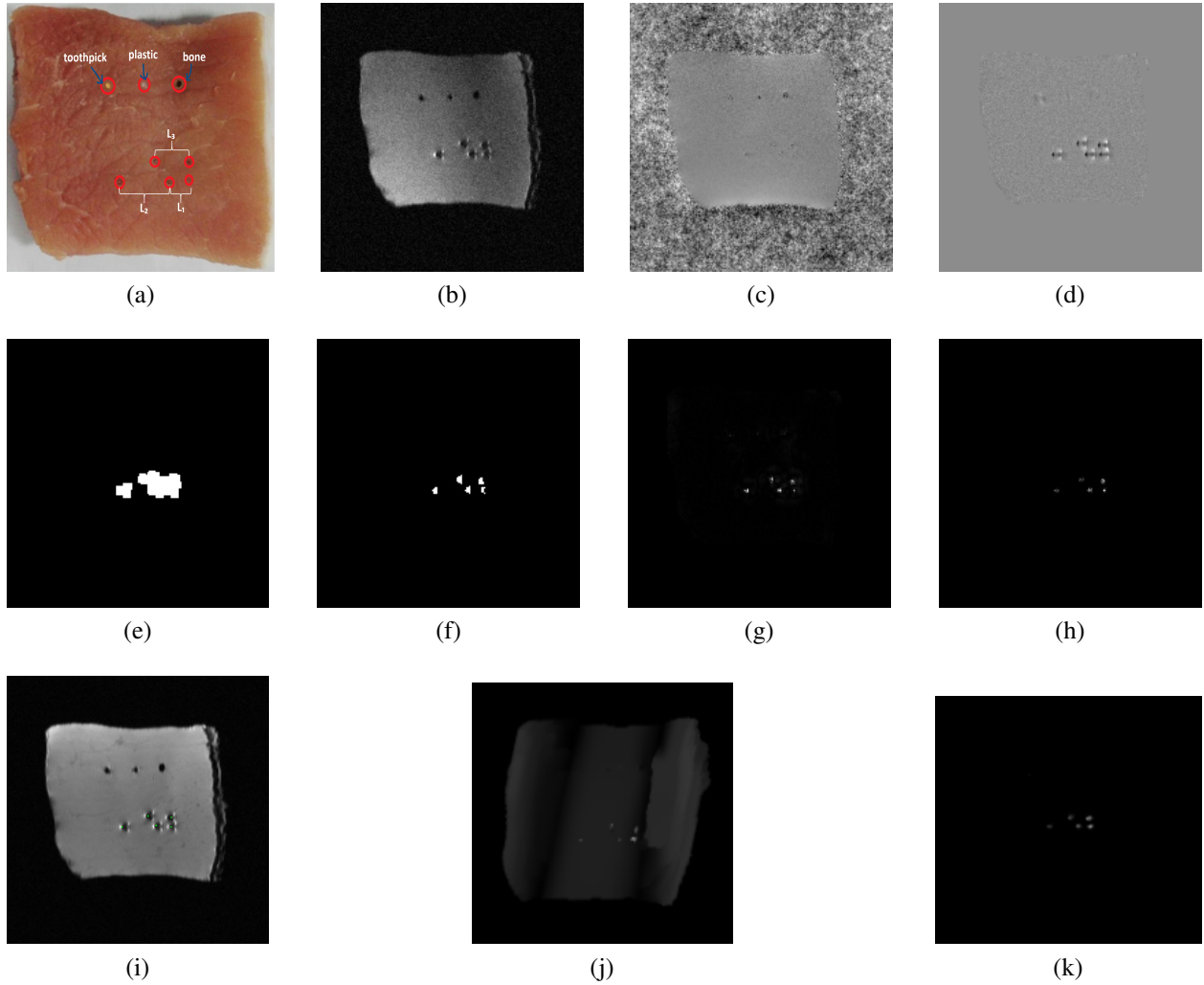
Figure 3.2: Reconstruction of Brachytherapy seeds from Seeds dataset (a) A picture of tissue phantom showing the positions of the brachytherapy seeds, bone, plastic stick and bamboo toothpick marked and labeled (b) Magnitude Image (c) Unwrapped Phase (d) Local Field Map (e) Local Field Mask (f) ROI (g) PCI generated using QSM (h) PCI generated using MARBLES (i) Seed locations marked in Magnitude Image (j) MIP for QSM based PCI (k) MIP for MARBLES based PCI

Figures 3.2e and 3.2f show the local field mask and ROI respectively. It can be observed from the local field (Figure 3.2d) and local field mask (Figure 3.2e) that the artifacts are formed only around the seed locations, while the other conflicting objects only form dark regions in the magnitude image. As a result, the ROI constructed (Figure 3.2f) is able to distinguish between the neighborhood regions of the seeds from the other dark regions. MARBLES is shown to locate

13

Table 3.1: Distance Comparisons

Actual Distance (mm)	Distance (MARBLES)			Distance (QSM)		
	pixels	mm	Error(mm)	pixels	mm	Error(mm)
L_1 (5mm)	11.04	6.90	1.90	10	6.25	1.25
L_2 (15mm)	25.02	15.64	0.64	26	16.25	1.25
L_1+L_2 (20mm)	36	22.50	2.50	36	22.50	2.50
L_3 (10mm)	17.03	10.64	0.64	16.12	10.07	0.07

all the five seeds in the dataset and was also able to differentiate between the target and other non-metallic simulated objects.

Figure 3.2i demonstrates the localization of all five brachytherapy seeds using MARBLES seen as green points marked on the magnitude image slice. Table 3.1 shows the comparison of the inter seed distances measured using the PCI obtained from MARBLES and QSM respectively, compared against the ground truth. The euclidean pixel distances were used to calculate the inter seed distances in the PCI and are converted to mm scale using the in-plane resolution for the dataset acquisition described in section 2.1.2. From the distance comparison, we see that the measured inter seed distances with MARBLES and QSM approaches were close to each other. The calculated distances were deviated from the ground truth by up to $1.25mm$, which translates to 2 pixels using the in-plane resolution for both approaches, showing similar performance with localization of the seeds. The MIP was used to compare the shape retention of the seeds. MIP comparison from figures 3.2j and 3.2k for both the QSM and SWI show that the shape of the seeds is preserved in case of MARBLES.

3.3 Experiments with Stent (Coronal) Dataset

Figure 3.3 demonstrates the results of using MARBLES approach on the stent coronal dataset. Stents have a mesh like structure, where the mesh orientation is not exactly parallel or perpendicu-

Figure 3.3: Reconstruction of Stent Coronal image for the Stent dataset (a) Magnitude Image (b) Unwrapped Phase (c) Local Field Map (d) PCI generated using QSM (e) PCI generated using MARBLES (f) MIP for QSM based PCI (g) MIP for MARBLES based PCI

lar to the magnetic field. Hence the results of the dataset can potentially demonstrate the influence of shape and orientation of metallic objects on the proposed method.

The magnitude image (figure 3.3a) shows the 8th slice, approximately the center slice of the dataset, calculated by the arithmetic average of all the 8 channels of the image. Figures 3.3b, 3.3c and 3.3d describe the unwrapped phase, calculated local field and PCI from the QSM respectively. Figure 3.3e shows the PCI constructed using MARBLES for the dataset, showing a coronal slice of the stent, as seen in figure 3.3e. MIP comparison of PCI for MARBLES and QSM, shown in figures 3.3g and 3.3f, demonstrate that the shape of the stent is retained with the MARBLES.

3.4 Experiments with Stent (Traversal) Dataset

Figure 3.4a shows the magnitude image of the 19th slice of the Stent Traversal dataset. The Magnitude image shown is the RMS of all the 8 channels of the image. Figures 3.4b, 3.4c and 3.4d describe the unwrapped phase, calculated local field and the PCI from the QSM respectively.
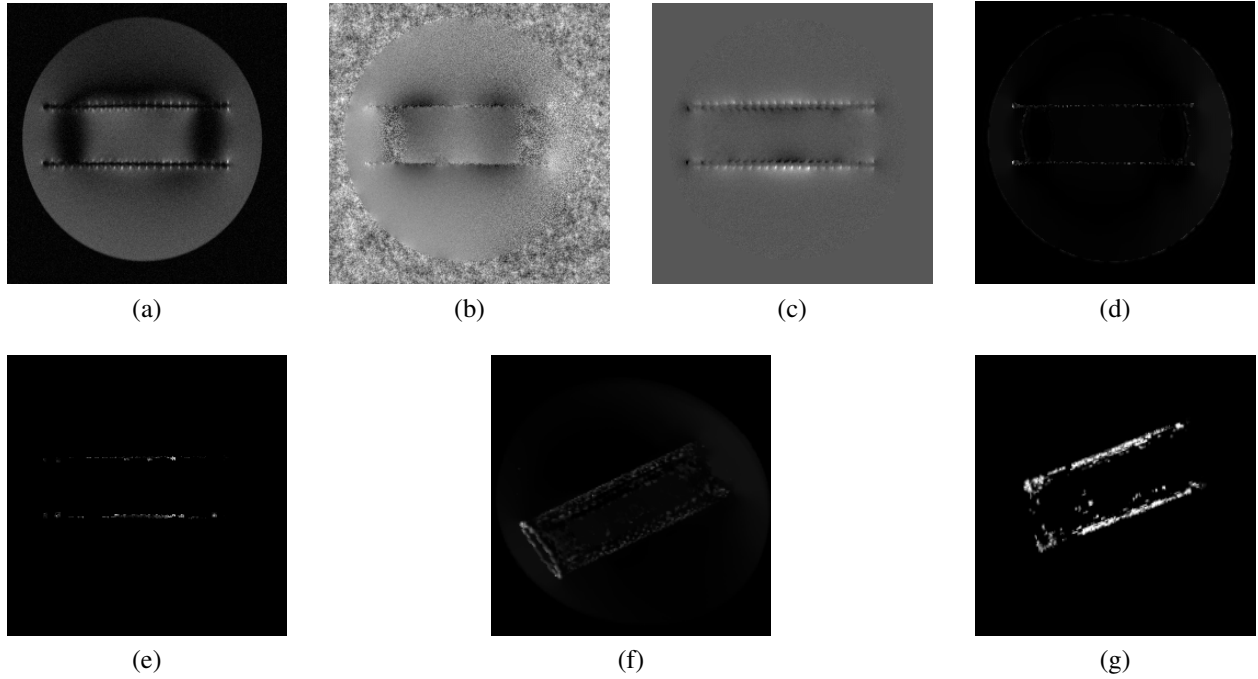
15
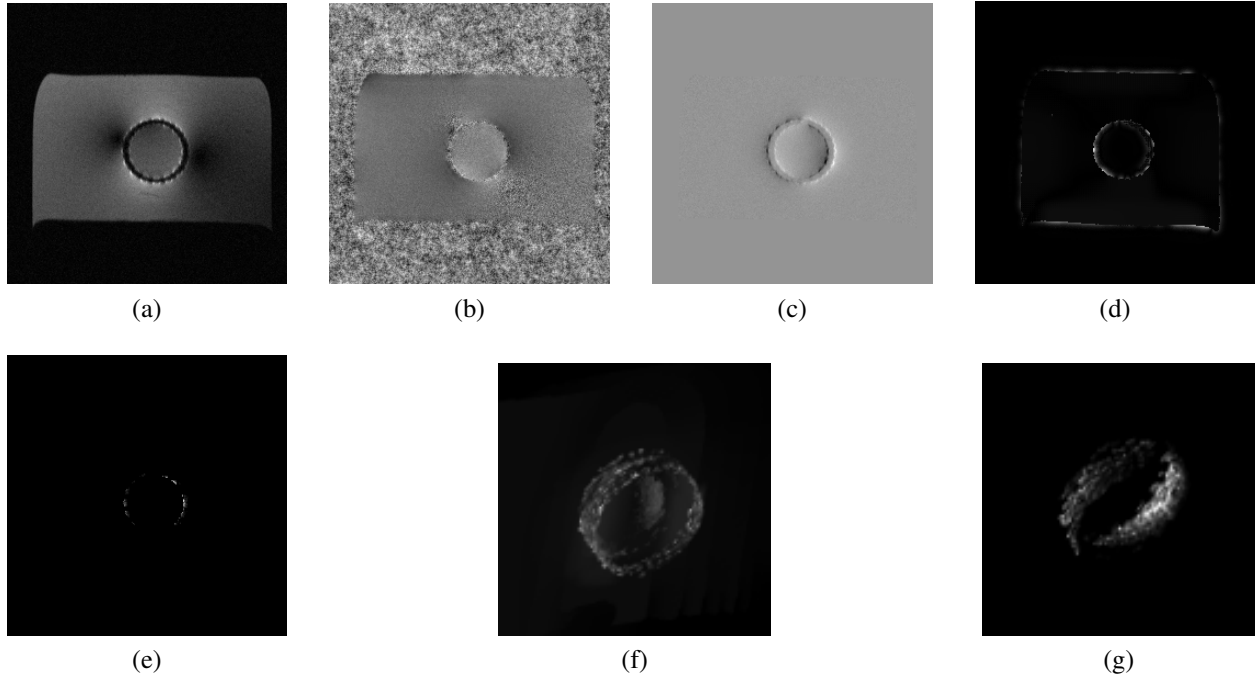
Figure 3.4: Reconstruction of Stent Traverse image for the Stent dataset (a) Magnitude Image (b) Unwrapped Phase (c) Local Field Map (d) PCI generated using QSM (e) PCI generated using MARBLES (f) MIP for QSM based PCI (g) MIP for MARBLES based PCI (zoom in view)

Figure 3.4e shows the PCI constructed using MARBLES for the dataset. On comparing the QSM and SWI slices in figures 3.4d and 3.4e, we see that the stent shown by the MARBLES retains the shape. Despite missing some parts of the circular cross section, the shape of the stent can be still seen form the MIP (see figure 3.4g), where the tube shape can be observed to be retained when compared to that of QSM based PCI (see figure 3.4f).

3.5 Computation Time Comparisons

Table 3.2 gives the comparison of PCI reconstruction times for QSM and MARBLES for the datasets 2.1.1, 2.1.2, 2.1.3, 2.1.4. PCI reconstruction with MARBLES was found to be 100.7, 109.9, 96.4 and 157.1 times faster than that of QSM for Biopsy Needle, Brachytherapy Seeds, Stent Coronal and Traversal datasets respectively, hence confirming our theoretical estimations in section 2.2.6. Thus the computation speed of PCI reconstruction construction with MARBLES is much faster than that of QSM.

Table 3.2: Comparison of PCI construction times for MARBLES vs. QSM

Dataset	PCI reconstruction time (seconds)		Speed-up factor
	QSM	MARBLES	
Biopsy Needle	88.61	0.88	100.7
Seeds	89.0	0.81	109.9
Stent(Coronal)	154.3	1.6	96.4
Stent(Traverse)	220.0	1.4	157.1

4. CONCLUSIONS

In this document, we proposed a new SWI based approach called Metal ARtifact Based Landmark Enhanced SWI (MARBLES) to visualize the metallic objects using MRI images. The method works by exploiting the locations of phase artifacts formed due to the metallic objects and uses them as landmarks to locate these objects. The method uses a phase mask in conjunction with an ROI constructed based on the location of the artifacts in the local field. MARBLES was found to be an effective and computationally faster approach for finding the locations of the metallic interventional devices. Experiments were performed on four datasets, while the results show that the approach was able to successfully localize the objects in the datasets.

Results from experiments 3.1, 3.2, 3.3 and 3.4 prove the shape retention of metallic objects with MARBLES when observed using MIP. The simpler computational approach made MARBLES to be computationally faster than the QSM approach. Hence we conclude that MARBLES is an alternative approach to the QSM-based method for visualizing smaller metallic devices such as brachetherapy seeds and biopsy needles in MRI due to its faster computation and acceptable performance.

REFERENCES

[1] M. Tatsuta, R. Yamamoto, H. Kasugai, Y. Okano, S. Noguchi, S. Okuda, A. Wada, and H. Tamura, "Cytohistologic diagnosis of neoplasms of the liver by ultrasonically guided fine-needle aspiration biopsy," *Cancer*, vol. 54, no. 8, pp. 1682–1686, 1984.

[2] Y. Tsutsumi, Y. Andoh, and N. Inoue, "Ultrasound-guided biopsy for deep-seated brain tumors," *Journal of neurosurgery*, vol. 57, no. 2, pp. 164–167, 1982.

[3] L. Liberman, "Percutaneous imaging-guided core breast biopsy: state of the art at the millennium," *American Journal of Roentgenology*, vol. 174, no. 5, pp. 1191–1199, 2000.

[4] L. Apesteguía and L. J. Pina, "Ultrasound-guided core-needle biopsy of breast lesions," *Insights into imaging*, vol. 2, no. 4, pp. 493–500, 2011.

[5] H. Holm, N. Juul, J. Pedersen, H. Hansen, and I. Strøyer, "Transperineal 125iodine seed implantation in prostatic cancer guided by transrectal ultrasonography," *The Journal of urology*, vol. 130, no. 2, pp. 283–286, 1983.

[6] S. Banerjee, T. Kataria, D. Gupta, S. Goyal, S. S. Bisht, T. Basu, and A. Abhishek, "Use of ultrasound in image-guided high-dose-rate brachytherapy: enumerations and arguments," *Journal of contemporary brachytherapy*, vol. 9, no. 2, p. 146, 2017.

[7] D. Kondziolka and L. Lunsford, "CT in image guided surgery," in *Textbook of Stereotactic and Functional Neurosurgery*, pp. 619–629, Springer, 2009.

[8] M. Knelson, J. Haaga, H. Lazarus, C. Ghosh, F. Abdul-Karim, and K. Sorenson, "Computed tomography-guided retroperitoneal biopsies.," *Journal of Clinical Oncology*, vol. 7, no. 8, pp. 1169–1173, 1989.

[9] S. H. Greenblatt, M. Rayport, E. R. Savolaine, J. H. Harris, and M. W. Hitchins, "Computed tomography-guided intracranial biopsy and cyst aspiration," *Neurosurgery*, vol. 11, no. 5, pp. 589–598, 1982.

[10] E. R. Savolaine, S. H. Greenblatt, and M. Rayport, "Computed tomography-guided intracranial biopsy and cyst aspiration: Accumulated experience in 60 patients," *Journal of Computed Tomography*, vol. 11, no. 3, pp. 221–227, 1987.

[11] J. H. Perry, A. E. Rosenbaum, D. L. Lunsford, C. A. Swink, and D. S. Zorub, "Computed tomography-guided stereotactic surgery: conception and development of a new stereotactic methodology," *Neurosurgery*, vol. 7, no. 4, pp. 376–381, 1980.

[12] J. J. Linde, K. F. Kofoed, M. Sørgaard, H. Kelbæk, G. B. Jensen, W. B. Nielsen, and J. D. Hove, "Cardiac computed tomography guided treatment strategy in patients with recent acute-onset chest pain: results from the randomised, controlled trial: Cardiac ct in the treatment of acute chest pain (catch)," *International journal of cardiology*, vol. 168, no. 6, pp. 5257–5262, 2013.

[13] J. Ricke and P. Wust, "Computed tomography–guided brachytherapy for liver cancer," in *Seminars in radiation oncology*, vol. 21, pp. 287–293, Elsevier, 2011.

[14] D. R. Simpson, D. J. Scanderbeg, R. Carmona, R. M. McMurtrie, J. Einck, L. K. Mell, M. T. McHale, C. C. Saenz, S. C. Plaxe, T. Harrison, *et al.*, "Clinical outcomes of computed tomography–based volumetric brachytherapy planning for cervical cancer," *International Journal of Radiation Oncologyâ Ăć Biologyâ Ăć Physics*, vol. 93, no. 1, pp. 150–157, 2015.

[15] L. Lunsford, R. Latchaw, and J. Vries, "Stereotactic implantation of deep brain electrodes using computed tomography," *Neurosurgery*, vol. 13, no. 3, pp. 280–286, 1983.

[16] S. A. Gulec, E. Hoenie, R. Hostetter, and D. Schwartzentruber, "PET probe-guided surgery: applications and clinical protocol," *World journal of surgical oncology*, vol. 5, no. 1, p. 65, 2007.

[17] L. L. Lin, S. Mutic, R. S. Malyapa, D. A. Low, T. R. Miller, M. Vicic, R. LaForest, I. Zoberi, and P. W. Grigsby, "Sequential FDG-PET brachytherapy treatment planning in carcinoma of

the cervix," *International Journal of Radiation Oncology* Biology* Physics*, vol. 63, no. 5, pp. 1494–1501, 2005.

[18] L. L. Lin, S. Mutic, D. A. Low, R. LaForest, M. Vicic, I. Zoberi, T. R. Miller, and P. W. Grigsby, "Adaptive brachytherapy treatment planning for cervical cancer using FDG-PET," *International Journal of Radiation Oncology* Biology* Physics*, vol. 67, no. 1, pp. 91–96, 2007.

[19] S. Thobois and E. Broussolle, "PET functional imaging of deep brain stimulation in parkinson's disease," *Journal of Neurolinguistics*, vol. 25, no. 2, pp. 133–138, 2012.

[20] P. Veit, C. Kuehle, T. Beyer, H. Kuehl, A. Bockisch, and G. Antoch, "Accuracy of combined PET/CT in image-guided interventions of liver lesions: an ex-vivo study," *World Journal of Gastroenterology: WJG*, vol. 12, no. 15, p. 2388, 2006.

[21] S. Nag, R. Martínez-Monge, R. Ellis, G. Lewandowski, L. Vacarello, J. G. Boutselis, and L. Copeland, "The use of fluoroscopy to guide needle placement in interstitial gynecological brachytherapy.," *International journal of radiation oncology, biology, physics*, vol. 40, no. 2, pp. 415–420, 1998.

[22] L. Liu, D. A. Bassano, S. C. Prasad, B. L. Keshler, and S. S. Hahn, "On the use of c-arm fluoroscopy for treatment planning in high dose rate brachytherapy," *Medical physics*, vol. 30, no. 9, pp. 2297–2302, 2003.

[23] B. D. Kavanagh, R. D. Zwicker, E. M. Segreti, L. A. Lindquist, A. S. Fulcher, G. M. Hundley, J. A. Spindler, and R. M. Cardinale, "Gynecologic brachytherapy: digital fluoroscopy for placement verification and treatment planning," *Radiology*, vol. 215, no. 3, pp. 900–903, 2000.

[24] A. Usman, F. Hussain, T. Iqbal, and F. Tuyyab, "Fluoroscopy time during cardiac catheterization procedures using the radial and femoral routes," *Journal of Ayub Medical College Abbottabad*, vol. 27, no. 3, pp. 569–572, 2015.

[25] S. M. Gyu, T. S. Seo, C. M. Park, J. W. Choi, J. M. Lee, and Y. S. Park, "Fluoroscopy guided transurethral placement of ureteral metallic stents," *Iranian Journal of Radiology*, vol. 12, no. 3, 2015.

[26] K. Ahrar, "Fluoroscopy-guided biopsy," in *Percutaneous Image-Guided Biopsy*, pp. 65–72, Springer, 2014.

[27] L. Kurban, L. Gomersall, J. Weir, and P. Wade, "Fluoroscopy-guided percutaneous lung biopsy: a valuable alternative to computed tomography," *Acta Radiologica*, vol. 49, no. 8, pp. 876–882, 2008.

[28] M. Mahesh, "Fluoroscopy: patient radiation exposure issues," *Radiographics*, vol. 21, no. 4, pp. 1033–1045, 2001.

[29] C. R. Merritt, "{CHAPTER} 21 - imaging techniques," in *Comprehensive Cytopathology (Third Edition)* (M. Bibbo and D. Wilbur, eds.), pp. 599 – 606, Edinburgh: W.B. Saunders, third edition ed., 2008.

[30] J. V. Frangioni, "New technologies for human cancer imaging," *Journal of clinical oncology*, vol. 26, no. 24, p. 4012, 2008.

[31] C. Wang, Z. Wang, T. Zhao, Y. Li, G. Huang, B. D. Sumer, and J. Gao, "Optical molecular imaging for tumor detection and image-guided surgery," *Biomaterials*, vol. 157, pp. 62–75, 2018.

[32] A. L. Vahrmeijer, M. Hutteman, J. R. Van Der Vorst, C. J. Van De Velde, and J. V. Frangioni, "Image-guided cancer surgery using near-infrared fluorescence," *Nature reviews Clinical oncology*, vol. 10, no. 9, p. 507, 2013.

[33] M. J. Landau, D. J. Gould, and K. M. Patel, "Advances in fluorescent-image guided surgery," *Annals of translational medicine*, vol. 4, no. 20, 2016.

[34] S. Keereweer, P. B. Van Driel, T. J. Snoeks, J. D. Kerrebijn, R. J. B. de Jong, A. L. Vahrmeijer, H. J. Sterenborg, and C. W. Löwik, "Optical image-guided cancer surgery: challenges and limitations," *Clinical Cancer Research*, vol. 19, no. 14, pp. 3745–3754, 2013.

[35] P. V. Houdek, J. G. Schwade, A. J. Medina, C. A. Poole, K. R. Olsen, D. H. Nicholson, S. Byrne, R. Quencer, R. S. Hinks, and V. Pisciotta, "MR technique for localization and verification procedures in episcleral brachytherapy," *International Journal of Radiation Oncology* Biology* Physics*, vol. 17, no. 5, pp. 1111–1114, 1989.

[36] D. McShan, R. Ten Haken, and B. Fraass, "3-D treatment planning: IV. integrated brachytherapy planning," *The use of computers in radiation therapy. North Holland: Elsevier Science Publishers BV*, pp. 249–252, 1987.

[37] Y. Kyuma, A. Hayashi, K. Odakiri, and H. Nakamae, "Basic study on MRI guided stereotaxic surgery," *No shinkei geka. Neurological surgery*, vol. 17, no. 5, pp. 449–455, 1989.

[38] C. Ménard, R. C. Susil, P. Choyke, G. S. Gustafson, W. Kammerer, H. Ning, R. W. Miller, K. L. Ullman, N. S. Crouse, S. Smith, *et al.*, "MRI-guided HDR prostate brachytherapy in standard 1.5 T scanner," *International Journal of Radiation Oncology* Biology* Physics*, vol. 59, no. 5, pp. 1414–1423, 2004.

[39] P. R. Arantes, E. F. Cardoso, M. A. Barreiros, M. J. Teixeira, M. R. Gonçalves, E. R. Barbosa, S. S. Sukwinder, C. C. Leite, and E. Amaro, "Performing functional magnetic resonance imaging in patients with parkinson's disease treated with deep brain stimulation," *Movement disorders*, vol. 21, no. 8, pp. 1154–1162, 2006.

[40] R. Bhidayasiri, J. M. Bronstein, S. Sinha, S. E. Krahl, S. Ahn, E. J. Behnke, M. S. Cohen, R. Frysinger, and F. G. Shellock, "Bilateral neurostimulation systems used for deep brain stimulation: in vitro study of MRI-related heating at 1.5 T and implications for clinical imaging of the brain," *Magnetic resonance imaging*, vol. 23, no. 4, pp. 549–555, 2005.

[41] M. Tagliati, J. Jankovic, F. Pagan, F. Susatia, I. U. Isaias, M. S. Okun, N. P. F. D. W. Group, *et al.*, "Safety of MRI in patients with implanted deep brain stimulation devices," *Neuroimage*, vol. 47, pp. T53–T57, 2009.

[42] M. E. Ladd, P. Erhart, J. F. Debatin, B. J. Romanowski, and G. C. McKinnon, "Biopsy needle susceptibility artifacts in magnetic resonance imaging," *Biomedizinische Technik/Biomedical*

Engineering, vol. 41, no. s1, pp. 202–203, 1996.

[43] A. Glowinski, G. Adam, A. Bucker, J. van Vaals, and R. Gunther, "A perspective on needle artifacts in MRI: an electromagnetic model for experimentally separating susceptibility effects," *IEEE transactions on medical imaging*, vol. 19, no. 12, pp. 1248–1252, 2000.

[44] G. Whitehead and J. Ji, "Positive contrast MRI of prostate brachytherapy seeds based on resonant frequency offset mapping," in *Engineering in Medicine and Biology Society (EMBC), 2010 Annual International Conference of the IEEE*, pp. 6641–6644, IEEE, 2010.

[45] M. A. Moerland, H. K. Wijrdeman, R. Beersma, C. J. Bakker, and J. J. Battermann, "Evaluation of permanent I-125 prostate implants using radiography and magnetic resonance imaging," *International Journal of Radiation Oncology* Biology* Physics*, vol. 37, no. 4, pp. 927–933, 1997.

[46] W. Lu, K. B. Pauly, G. E. Gold, J. M. Pauly, and B. A. Hargreaves, "SEMAC: slice encoding for metal artifact correction in MRI," *Magnetic resonance in medicine*, vol. 62, no. 1, pp. 66–76, 2009.

[47] K. M. Koch, J. E. Lorbiecki, R. S. Hinks, and K. F. King, "A multispectral three-dimensional acquisition technique for imaging near metal implants," *Magnetic resonance in medicine*, vol. 61, no. 2, pp. 381–390, 2009.

[48] Y. H. Lee, D. Lim, E. Kim, S. Kim, H.-T. Song, and J.-S. Suh, "Usefulness of slice encoding for metal artifact correction (SEMAC) for reducing metallic artifacts in 3-T MRI," *Magnetic resonance imaging*, vol. 31, no. 5, pp. 703–706, 2013.

[49] P. R. Seevinck, H. de Leeuw, C. Bos, and C. J. Bakker, "Highly localized positive contrast of small paramagnetic objects using 3D center-out radial sampling with off-resonance reception," *Magnetic resonance in medicine*, vol. 65, no. 1, pp. 146–156, 2011.

[50] M. Stuber, W. D. Gilson, M. Schär, D. A. Kedziorek, L. V. Hofmann, S. Shah, E.-J. Vonken, J. W. Bulte, and D. L. Kraitchman, "Positive contrast visualization of iron oxide-labeled

stem cells using inversion-recovery with ON-resonant water suppression (IRON),” *Magnetic Resonance in Medicine*, vol. 58, no. 5, pp. 1072–1077, 2007.

[51] H. De Leeuw, P. Seevinck, and C. Bakker, “Center-out radial sampling with off-resonant reconstruction for efficient and accurate localization of punctate and elongated paramagnetic structures,” *Magnetic resonance in medicine*, vol. 69, no. 6, pp. 1611–1622, 2013.

[52] H. Dahnke, W. Liu, D. Herzka, J. A. Frank, and T. Schaeffter, “Susceptibility gradient mapping (SGM): A new postprocessing method for positive contrast generation applied to superparamagnetic iron oxide particle (SPIO)-labeled cells,” *Magnetic resonance in medicine*, vol. 60, no. 3, pp. 595–603, 2008.

[53] G. Varma, R. E. Clough, P. Acher, J. Sénégas, H. Dahnke, S. F. Keevil, and T. Schaeffter, “Positive visualization of implanted devices with susceptibility gradient mapping using the original resolution,” *Magnetic resonance in medicine*, vol. 65, no. 5, pp. 1483–1490, 2011.

[54] L. De Rochefort, R. Brown, M. R. Prince, and Y. Wang, “Quantitative MR susceptibility mapping using piece-wise constant regularized inversion of the magnetic field,” *Magnetic Resonance in Medicine*, vol. 60, no. 4, pp. 1003–1009, 2008.

[55] L. De Rochefort, T. Liu, B. Kressler, J. Liu, P. Spincemaille, V. Lebon, J. Wu, and Y. Wang, “Quantitative susceptibility map reconstruction from MR phase data using bayesian regularization: validation and application to brain imaging,” *Magnetic Resonance in Medicine*, vol. 63, no. 1, pp. 194–206, 2010.

[56] J. Acosta-Cabronero, G. B. Williams, A. Cardenas-Blanco, R. J. Arnold, V. Lupson, and P. J. Nestor, “In-vivo quantitative susceptibility mapping (QSM) in alzheimer’s disease,” *PloS one*, vol. 8, no. 11, p. e81093, 2013.

[57] Y. Dong, Z. Chang, G. Xie, G. Whitehead, and J. X. Ji, “Susceptibility-based positive contrast MRI of brachytherapy seeds,” *Magnetic resonance in medicine*, vol. 74, no. 3, pp. 716–726, 2015.

[58] Y. Dong, Z. Chang, and J. Ji, "Imaging and localizing interventional devices by susceptibility mapping using MRI," in *Engineering in Medicine and Biology Society (EMBC), 2014 36th Annual International Conference of the IEEE*, pp. 1541–1544, IEEE, 2014.

[59] C. Shi, G. Xie, Y. Zhang, X. Zhang, M. Chen, S. Su, Y. Dong, X. Liu, and J. Ji, "Accelerated susceptibility-based positive contrast imaging of MR compatible metallic devices based on modified fast spin echo sequences," *Physics in Medicine and Biology*, vol. 62, no. 7, p. 2505, 2017.

[60] S. Liu, S. Buch, Y. Chen, H.-S. Choi, Y. Dai, C. Habib, J. Hu, J.-Y. Jung, Y. Luo, D. Utriainen, *et al.*, "Susceptibility-weighted imaging: current status and future directions," *NMR in Biomedicine*, vol. 30, no. 4, 2017.

[61] E. M. Haacke, Y. Xu, Y.-C. N. Cheng, and J. R. Reichenbach, "Susceptibility weighted imaging (SWI)," *Magnetic resonance in medicine*, vol. 52, no. 3, pp. 612–618, 2004.

[62] E. M. Haacke, S. Mittal, Z. Wu, J. Neelavalli, and Y.-C. Cheng, "Susceptibility-weighted imaging: technical aspects and clinical applications, part 1," *American Journal of Neuroradiology*, vol. 30, no. 1, pp. 19–30, 2009.

[63] S. Mittal, Z. Wu, J. Neelavalli, and E. M. Haacke, "Susceptibility-weighted imaging: technical aspects and clinical applications, part 2," *American Journal of neuroradiology*, vol. 30, no. 2, pp. 232–252, 2009.

[64] M. Miquel, K. Rhode, P. Acher, N. MacDougall, J. Blackall, R. Gaston, S. Hegde, S. Morris, R. Beaney, C. Deehan, *et al.*, "Using combined X-ray and MR imaging for prostate I-125 post-implant dosimetry: phantom validation and preliminary patient work," *Physics in medicine and biology*, vol. 51, no. 5, p. 1129, 2006.

[65] J. F. Schenck, "The role of magnetic susceptibility in magnetic resonance imaging: MRI magnetic compatibility of the first and second kinds," *Medical physics*, vol. 23, no. 6, pp. 815–850, 1996.

[66] K. Wachowicz, S. Thomas, and B. Fallone, "Characterization of the susceptibility artifact around a prostate brachytherapy seed in MRI," *Medical physics*, vol. 33, no. 12, pp. 4459–4467, 2006.

[67] V. Lagerburg, M. Moerland, J. Seppenwoolde, and J. Lagendijk, "Simulation of the artefact of an iodine seed placed at the needle tip in MRI-guided prostate brachytherapy," *Physics in medicine and biology*, vol. 53, no. 5, p. N59, 2008.

[68] S. Thomas, K. Wachowicz, and B. Fallone, "MRI of prostate brachytherapy seeds at high field: a study in phantom," *Medical physics*, vol. 36, no. 11, pp. 5228–5234, 2009.

[69] D. Zhou, T. Liu, P. Spincemaille, and Y. Wang, "Background field removal by solving the laplacian boundary value problem," *NMR in Biomedicine*, vol. 27, no. 3, pp. 312–319, 2014.

[70] Y. Wang, Y. Yu, D. Li, K. Bae, J. Brown, W. Lin, and E. Haacke, "Artery and vein separation using susceptibility-dependent phase in contrast-enhanced MRA," *Journal of Magnetic Resonance Imaging*, vol. 12, no. 5, pp. 661–670, 2000.

[71] M. Lustig, D. Donoho, and J. M. Pauly, "Sparse MRI: The application of compressed sensing for rapid MR imaging," *Magnetic resonance in medicine*, vol. 58, no. 6, pp. 1182–1195, 2007.

APPENDIX A

COMPUTATIONAL COMPLEXITY CALCULATIONS FOR QSM APPROACH

A.1 Convex optimization solution for QSM

The description of the QSM algorithm in [57] was used to solve the equation described by equation (1.1). The approach solves the problem by setting first order derivative of (1.1) to 0, given by

$$\frac{\partial f}{\partial \chi} = 2C^H W^H (W(C\chi - \Delta B)) + \lambda \nabla ||MG\chi||_1 = 0 \tag{A.1}$$

Where, ^{H} is Hermitian operator. Since $||MG\chi||_1$ is discontinuous at 0, we add a small regularization number μ to make it continuous and differentiable at 0 [71]. Hence the derivative is simplified to

$$\frac{\partial f}{\partial \chi} = 2C^H W^H (W(C\chi - \Delta B)) + \lambda G^H M^H T^{-1} MG\chi = 0 \tag{A.2}$$

where T is a diagonal matrix with $t_k = \sqrt{(MG\chi)_k^H (MG\chi)_k + \mu}$ as its diagonal entries. The value of μ was set to 10^{-15} experimentally. A non-linear conjugate gradient solver (CGS) was employed to iteratively solve the equation A.2.

A.2 Computational Complexity Calculations

The terms in equation (A.2) are calculated in every iteration of the CGS. Hence, in order to estimate the complexity of the CGS, the complexity for computing each term in the equation (A.2) was first estimated.

The size of the MR image is assumed to be N for the calculations. The dipole kernel convolution operator in equation (A.2) can be expanded as $C = F^{-1}DF$, where F and F^{-1} are Fast Fourier and its inverse operator respectively and D is the dipole kernel operator in k-space. The FFT and IFFT operations are of the complexity $O(N \log N)$ and element wise multiplication with dipole

kernel D is of the complexity $O(N)$. So the complexity for calculating the dipole kernel convolution operations C and C^H is $O(N \log N) + O(N \log N) + O(N) = O(N \log N)$. The weight operator W operates as element wise multiplication, so its complexity is $O(N)$. Hence the complexity for calculating the first term is $O(N \log N) + O(N) + O(N) + O(N \log N) = O(N \log N)$.

The gradient operation G only involves a circular shift and an arithmetic subtraction, and hence its operation complexity is $O(1)$. The mask M operates with complexity order $O(N)$ as it operates as element-wise multiplication. Thus, the complexity for calculating $MG\chi$ is $O(N) + O(1) = O(N)$. Also, element-wise square root is an $O(N)$ operation. Hence the complexity for computing T is $O(N) + O(N) + O(N) = O(N)$.

Hence computational complexity of second term of (A.2) is $O(N) + O(N) + O(N) = O(N)$. The total complexity for calculating the terms in (A.2) is $O(N) + O(N \log N) = O(N \log N)$.

That assuming p to be the number of operator calls made to calculate terms in equation (A.2), the total complexity order for computing PCI using QSM is $O(pN \log N)$.